

Blood Flow Reduction in Breast Tissue due to Mammographic Compression

David R. Busch, PhD, Regine Choe, PhD, Turgut Durduran, PhD, Daniel H. Friedman, Wesley B. Baker, MSci, Andrew D. Maidment, PhD, Mark A. Rosen, MD, PhD, Mitchell D. Schnall, MD, PhD, Arjun G. Yodh, PhD

Rationale and objectives: This study measures hemodynamic properties such as blood flow and hemoglobin concentration and oxygenation in the healthy human breast under a wide range of compressive loads. Because many breast-imaging technologies derive contrast from the deformed breast, these load-dependent vascular responses affect contrast agent-enhanced and hemoglobin-based breast imaging.

Methods: Diffuse optical and diffuse correlation spectroscopies were used to measure the concentrations of oxygenated and deoxygenated hemoglobin, lipid, water, and microvascular blood flow during axial breast compression in the parallel-plate transmission geometry.

Results: Significant reductions ($P < .01$) in total hemoglobin concentration (~30%), blood oxygenation (~20%), and blood flow (~87%) were observed under applied pressures (forces) of up to 30 kPa (120 N) in 15 subjects. Lipid and water concentrations changed <10%.

Conclusions: Imaging protocols based on injected contrast agents should account for variation in tissue blood flow due to mammographic compression. Similarly, imaging techniques that depend on endogenous blood contrasts will be affected by breast compression during imaging.

Key Words: Mammographic compression; breast cancer; blood flow; breast imaging; diffuse optics.

©AUR, 2014

Exogenous contrast agents are playing an increasingly important role in breast cancer screening and diagnosis, because they improve image signal-to-noise and offer novel targeting potential as tissue biomarkers. Dynamic contrast-enhanced magnetic resonance imaging (DCE-MRI) uses intravenous injection of gadolinium-diethylenetriamine pentaacetic acid (Gd-DTPA), for example, and is currently recommended as a screening tool for high-risk women (1). Similarly, contrast-enhanced digital x-ray tomosynthesis often uses injection of iodine-based agents into the compressed breast (2,3). Both of these techniques rely on adequate blood flow to control the delivery, uptake, and spatial distribution of the contrast

agent. Deformation of breast tissue during compression, however, can lead to modifications of regional blood flow that alter tissue oxygenation and metabolism as well as contrast agent delivery. Furthermore, the mechanical properties of tumors are generally different from those of the surrounding tissues (4–12), and these differences can lead to uncontrolled and heterogeneous vascular responses of the breast to compression. Thus, compression can significantly reduce cancer contrast.

In addition to the standard clinical techniques mentioned previously, scientists continue to explore new technologies to enhance breast cancer specificity and sensitivity. Diffuse optical spectroscopy (DOS) and tomography (DOT), for example, are novel methodologies that utilize photons in the near-infrared (NIR, 650–950 nm) tissue transmission window to measure properties of normal and diseased breast tissues non-invasively and *in vivo* (13–39). In breast cancer, these physiological parameters typically include the concentration of oxygenated and deoxygenated hemoglobin (HbO_2 and Hb , respectively), from which total tissue hemoglobin concentration ($\text{Hb}_t = \text{HbO}_2 + \text{Hb} \propto \text{blood volume}$) and blood oxygen saturation ($\text{StO}_2 = \text{HbO}_2/\text{Hb}_t$) are readily calculated. These hemodynamic parameters, including other tissue properties such as water and lipid concentration and reduced tissue scattering (μ'_s), all provide significant endogenous tumor contrast for the optical method. In

Acad Radiol 2014; 21:151–161

From the Division of Neurology, Children's Hospital of Philadelphia, Department of Physics and Astronomy, University of Pennsylvania, Philadelphia, PA, 19104 (D.R.B.); Department of Biomedical Engineering, University of Rochester, Rochester, NY (R.C.); ICFO-Institut de Ciències Fotòniques, Castelldefels (Barcelona), Spain (T.D.); Department of Mechanical Engineering and Applied Mechanics (D.H.F.); Department of Physics and Astronomy, University of Pennsylvania, Philadelphia, PA (W.B., A.G.Y.); and Department of Radiology, Hospital of the University of Pennsylvania, Philadelphia, PA (A.D.M., M.A.R., M.D.S.). Received August 17, 2013; accepted October 14, 2013. **Address correspondence to:** D.R.B. e-mail: drbusch@sdf.org

©AUR, 2014

<http://dx.doi.org/10.1016/j.acra.2013.10.009>

practice, clinical DOS/DOT measurements typically involve placing breast tissue under some type of mild compression, however, and the effects of this compression on breast tissue vasculature are not generally considered in the analysis of DOT results, despite observations suggesting that compression effects are present (24,30,40–48).

In light of these issues concerning hemodynamics and contrast agent delivery, the primary focus of the present article is to characterize the blood flow responses of healthy breast tissue to compression. We use a compression similar to that performed in clinical mammograms and in contrast-enhanced x-ray tomosynthesis—that is, a parallel-plate geometry with applied loads up to 120 N. Importantly, the data derived provide the first direct measurements of microvascular blood flow changes during compression and provide insight about healthy breast tissue hemodynamic responses to compression. Ultimately, these results should provide guidance for use of contrast agents to enhance tumor visibility in the compressed breast and for optimal implementation of DOT and DOS.

To accomplish this goal, DOS is used for the measurement of average tissue chromophore concentrations, and a relatively new technique, diffuse correlation spectroscopy (DCS), is used for direct measurement of microvascular breast tissue blood flow (14,49–60). Briefly, DCS measures fluctuations in light intensity collected after transmission through the breast. These temporal fluctuations depend on the flow of red blood cells. Larger flows yield faster fluctuations of the detected light field and a more rapid decay of the field temporal autocorrelation function. DCS blood flow indices (BF) are derived from the measured temporal decay rate of the autocorrelation function; the flow indices have been validated previously (61–74). Notably, the study described here also represents the first DCS-flow measurements detected in *transmission* through human breast, and because full tomographic diffuse optical reconstruction of breast generally requires *transmission* measurements, the study takes an important first step toward optical blood flow *tomography* of human breast.

METHODS

Recruitment

A total of 30 healthy volunteers over the age of 18 years were recruited. Because of mechanical limitations of our tissue interface, we initially restricted recruitment to women who wore B-cup or larger bras; after gaining experience with measurements, we limited further recruitment to women with C-cup or larger bras (patient demographics are described in Table 1). Five subjects were not included in analysis because of motion artifacts or tissue contact issues; eight subjects were excluded because of low DCS signal; and two subjects were excluded because of instrumental mechanical failure. Partial datasets, however (e.g., the left breast of a woman who moved during right breast measurements), were included in the analysis. Thus, the data reported are derived from 15 healthy volunteers.

TABLE 1. Demographic Information for Healthy Subjects Studied in the Compression Investigation

Parameters	Subjects (N = 15)
Age, yr	35 ± 16 (19, 67)
BMI, kg/m ²	26 ± 7.8 (19.6, 49.3)
Menopausal status	
Premenopausal	12 (75%)
Postmenopausal	3 (25%)
Bra cup size	
B	1 (7%)
C	8 (53%)
D	5 (33%)
E	1 (7%)
Race/ethnicity	
Caucasian	11 (73%)
African American	3 (20%)
Asian	1 (7%)
Hispanic	0 (0%)

Race/ethnicity and bra cup size are self-reported. Body mass index (BMI) and age are reported as mean ± standard deviation (minimum, maximum).

Measurement Protocol

After the instrument height was properly adjusted for each subject (Fig 1a), baseline measurements of force (load), pressure, and optical properties were collected. Optical measurements utilized a time-domain DOS (TD-DOS) system. The TD-DOS instrument consisted of 690, 750, 785, 800, 830, and 838 nm pulsed diode lasers (Picoquant, Berlin Germany), photon-counting photomultiplier tubes (H7422-50P, Hamamatsu, Hamamatsu City, Japan), and time-correlated single photon-counting electronics (SPC-134, Becker and Hickl, Berlin, Germany), all described in Busch (75). The blood flow measurements were carried out with the DCS technique using a light source at 785 nm and detectors described in Durduran et al. (62). We used a single source and detector position for the optical measurements, colocating and averaging eight DCS detectors to improve the signal-to-noise ratio (SNR). Optical measurements were performed serially; TD-DOS measurements at all six wavelengths were followed by DCS measurements at a single wavelength. Integration times for each technique were adjusted to provide acceptable SNR for each technique; the TD-DOS wavelength was integrated for ~1–2 seconds at the baseline plate separation and ~0.5–1 seconds during compression; DCS signal was integrated for ~3–5 seconds throughout the experiment. The integration times were chosen generously to improve SNR; in the future, various technical alterations should permit faster data acquisition.

Skin pressure was measured using an array of 26 sensors (Tactilus Free Form, Sensor Products, Madison, NJ) distributed on the upper and lower compression plates (Fig 1b,c). The pressure readings across the breast were highly heterogeneous due to edge effects; therefore, we used three sensors immediately adjacent to the fiber optics, that is, close to the location where the breast was centered, for further analysis.

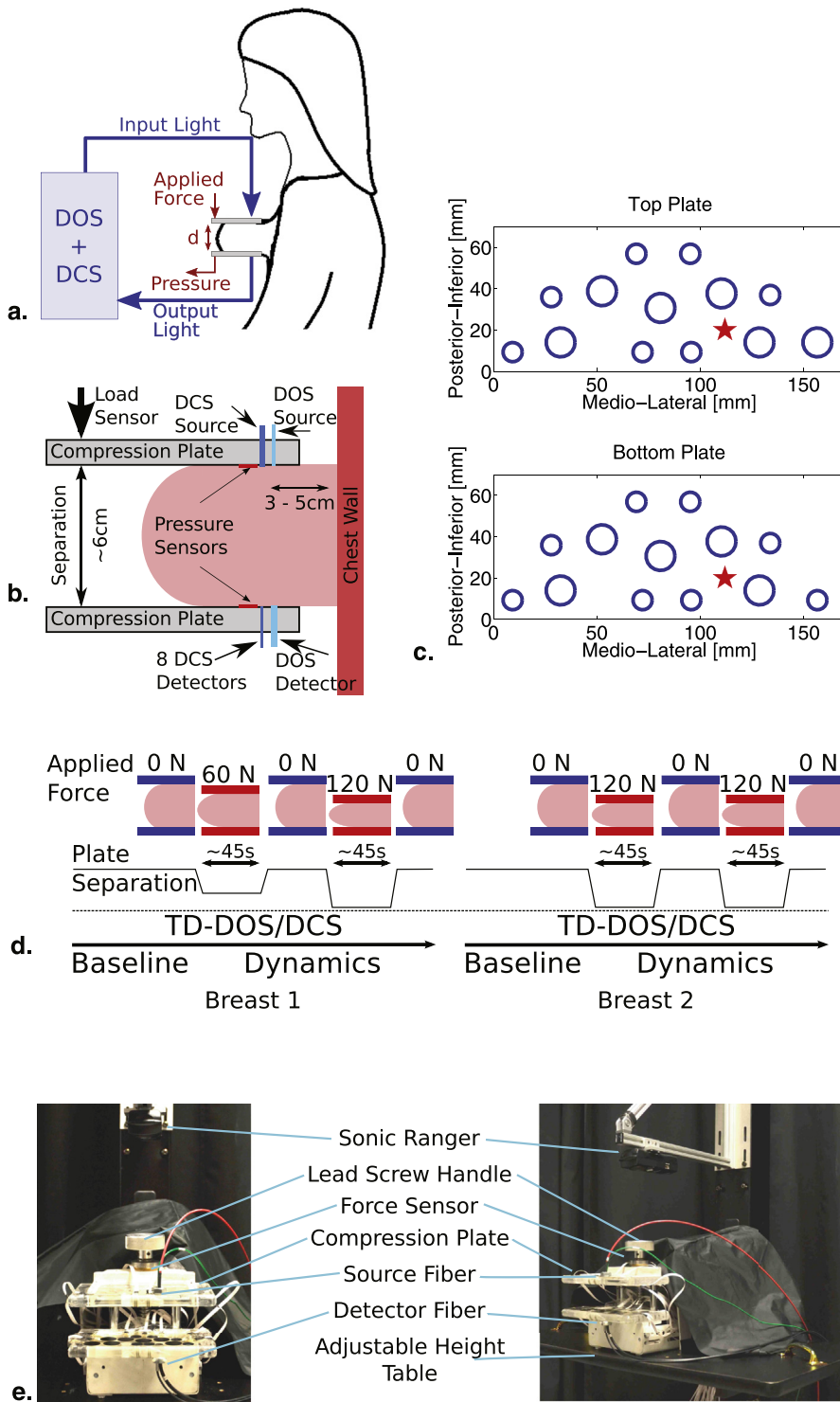


Figure 1. (a) Schematic overview. The subject is seated on a height-adjustable chair with the breast placed between two compression plates. Optical fibers couple light into and out of the tissue and are also coupled to the optoelectronics of the combined diffuse optical/diffuse correlation spectroscopy (DOS/DCS) instrument module. Skin pressure (P), applied force (F), and plate separation (d) are measured throughout the study. (b) Schematic view of compression plates, load sensor, pressure sensor, and optodes. To improve data quality, eight DCS detectors were co-located and data from these detectors were obtained in parallel and averaged. Twenty-six pressure sensors were located on the upper and lower plates. (c) Schematic view of pressure sensor distribution. The red star indicates the optode location. The size of the blue circles denotes the size of the sensor (15- or 25-mm diameter; size is proportional to sensitivity). (d) Experimental timeline. The initial compression was set to a nominal force of 60 N, and the subsequent compressions were set to ~ 120 N. In practice, both of these force levels were limited by subject compliance. (e) Photograph of compression plate system. For interpretation of the references to color in this figure legend, the reader is referred to the web version of this article.

The applied force was measured with a load sensor (LC8200-625-50, Omega Engineering, Swedesboro, NJ). Load and pressure sensors were calibrated daily.

We first applied a step compression to ~ 60 N force or the maximum permitted by the subject; we refer to this step as a partial compression. After partial compression, the data were collected for ~ 45 seconds, and then the plate configuration

was returned to the baseline separation, which we refer to as the relaxed configuration. After ~ 90 seconds, we then applied a step compression of ~ 120 N or maximum permitted by the subject; we refer to this step as a full compression. After full compression, the data were collected for ~ 45 seconds, and the plate configuration was again returned to the baseline separation. We then repositioned the subject's other breast within

the instrument, and we repeated the sequence of steps described previously, except that this time our goal was to apply 120 N during both repetitions (76). In designing this protocol, we attempted to capture both a graded response (partial versus complete) and hysteresis effects—for example, changes due to repeated complete compression. In practice, subject compliance and tissue relaxation under load reduced the average applied force in the partial compression time-windows to ~15–60 N and reduced the applied force in the full compression time-windows to ~60–120 N. As a result of these variations, an almost continuous range of compression forces were applied across our subject population. Furthermore, we could not discern a hysteresis effect with repeated compression across this subject population.

The speed of compression application was limited by both patient compliance and by the manually driven controls in the device. A timeline of the process is shown in Fig 1d. After setting the initial load, the plate separation was held constant for the remainder of the measurement time, that is, the data were obtained at constant plate separation, rather than constant load. Plate separation was initially measured by hand during each compression period using a caliper, and subsequently it was continuously monitored using an ultrasonic ranging device (Go!Motion, Vernier Software and Technology, Beaverton, OR).

If subjects expressed discomfort, the study was terminated. Data were also excluded if the subject moved during the measurement or moved during the time between the baseline and compression measurements. Partial datasets, for example, from one breast, were included in our analysis.

Chromophore concentrations (HbO₂, Hb, lipid, and water [H₂O]) were simultaneously fit to six-wavelength TD-DOS data using a multispectral algorithm. In this analysis, the free parameters were the concentrations of HbO₂, Hb, lipid, and H₂O, as well as two parameters (*A* and *b*) modeling the scattering coefficient (77) by the power law:

$$\mu'_s(\lambda) = A\lambda^{-b} \quad (1)$$

for each optical wavelength λ (nm). Note that μ'_s and the quantity ($A\lambda^{-b}$) have units of cm^{-1} . The tissue absorption coefficient is a sum of terms containing both the *i*th chromophore concentration (C_i , mol/L) and their respective extinction coefficients (ϵ_i , $\text{cm}^{-1} \text{mol}^{-1} \text{L}$), that is,

$$\mu_a(\lambda) = \sum_i C_i \cdot \epsilon_i(\lambda) \cdot \ln(10) \quad (2)$$

where the sum is over all tissue chromophores and μ_a has units of cm^{-1} . Additionally, two derived parameters, total hemoglobin concentration and blood oxygen saturation, were calculated at each time point.

The DCS temporal intensity autocorrelation functions were fit to the standard infinite slab solution of the correlation diffusion equation, using the optical properties determined by the TD-DOS measurements. The blood flow index, BF, is thus derived from best fits of the theory to the temporal decay of

the autocorrelation function; we note that changes in such indices have been validated previously in a variety of tissues under several different perturbations (61–74). Additional details of the TD-DOS and DCS analysis are provided in the Appendix.

For the purposes of intersubject comparison, we normalized measured parameters for each subject to reduce the impact of individual subject physiology. For example, Hb_{*t*} can vary widely between subjects (33). We therefore examined the relative changes (denoted by a prefactor, *r*) from baseline in each parameter. Specifically, we define

$$r\text{Hb}_t = \frac{\text{Hb}_t}{(\text{Hb}_t)_0}$$

$$\Delta\text{StO}_2 = \text{StO}_2 - (\text{StO}_2)_0$$

$$r\text{BF} = \frac{\text{BF}}{\text{BF}_0}$$

$$\Delta\text{Lipid} = \text{Lipid} - \text{Lipid}_0$$

$$\Delta\text{H}_2\text{O} = \text{H}_2\text{O} - (\text{H}_2\text{O})_0$$

$$r\mu'_s = \frac{\mu'_s}{(\mu'_s)_0}$$

$$\Delta P = P - P_0$$

$$\Delta F = F - F_0$$

where the resulting normalized physiological parameters are measured in percentages (or as differences) relative to the baseline (X_0) value.

Statistical Methods

The variation of each measured parameter (e.g., blood flow, hemoglobin concentration) from baseline was determined for each repetition of each subject. These data were then binned by applied pressure or applied force, that is, baseline, 0–10, 10–20, and 20–30 kPa and baseline, 0–30, 30–60, 60–90, and 90–120 N, respectively. For each parameter, we tested the hypothesis that the compression-induced change was significantly different from baseline using a two-tailed Student *t* test.

This study was conducted under a protocol approved by the Institutional Safety Review Board of the University of Pennsylvania.

RESULTS

Example Data from Individual Subjects

Typical results from a single subject are shown in Figs 2 and 3. Plate separation (*d*) was held constant for the duration of each time-window. In the time-windows wherein the breast is compressed (Fig 2a), the measured force was observed to quickly decrease after the compression plate ceased moving (Fig 2b). The measured pressure at the skin surface (Fig 2b) showed a similar pattern. These effects may be due to mechanical relaxation of the tissue and/or redistribution of fluid within tissue compartments. Physiological and

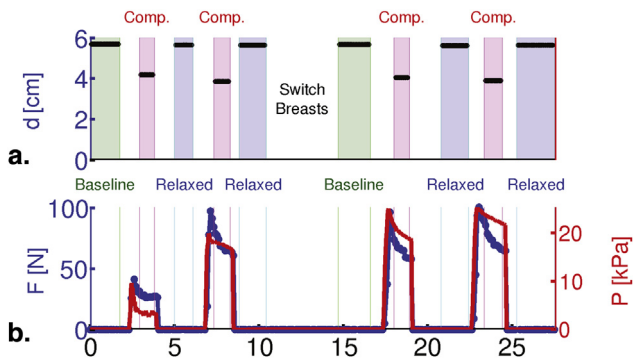


Figure 2. Example data from a 28-year-old subject (body mass index = 19.6 kg/m²), showing time traces of distance, force, and pressure. **(a)** Plate separation (d). **(b)** Applied force (F , blue, left axis) and surface pressure (P , red, right axis). The plate separation d is inversely related to force (F) and pressure (P). Hemodynamic measurements for this subject are shown in Figure 3. For interpretation of the references to color in this figure legend, the reader is referred to the web version of this article.

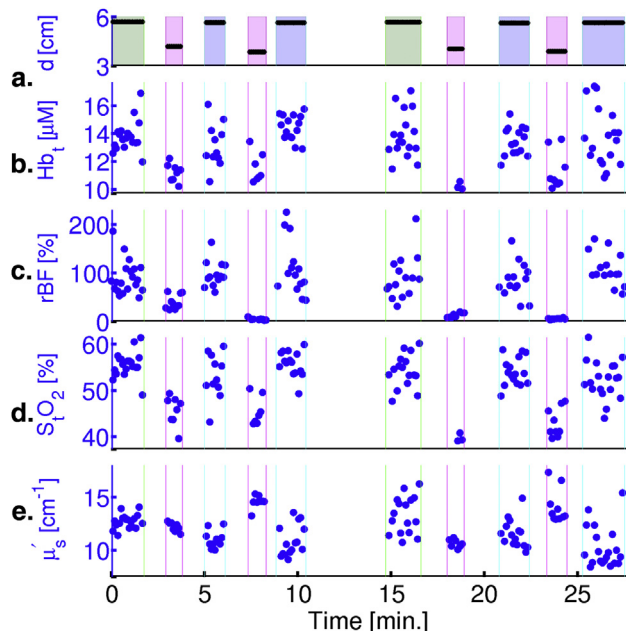


Figure 3. Example data from a 28-year-old subject (body mass index = 19.6 kg/m²), showing time traces of distance and hemodynamic properties. Mechanical measurements for this subject are shown in Figure 2. **(a)** Plate separation (d). **(b)** Total hemoglobin concentration (Hb_t). **(c)** Relative blood flow (rBF). **(d)** Blood oxygen saturation (StO_2) and **(e)** reduced tissue scattering coefficient μ'_s versus experiment time. As expected, Hb_t (**b**), rBF (**c**), and StO_2 (**d**) are reduced during compression. For interpretation of the references to color in this figure legend, the reader is referred to the web version of this article.

mechanical properties of the tissue were recorded continuously during the measurement of each breast with frame rate determined by the integration time necessary for sufficient SNR in each subject (~ 0.1 – 0.2 Hz); recordings of applied force and pressure were downsampled to this rate. Although we attempted to reach 60 N during the partial compression period and 120 N during the full compression period, these

force levels were limited by subject compliance. For example, as seen in Fig 2b, this particular subject accepted a partial compression of ~ 45 N and a full compression of ~ 100 N.

Total hemoglobin content (Hb_t , Fig 3b) decreased by up to 30% compared to baseline during the high-load periods. Relative blood flow ($rBF = BF/BF_0$, Fig 3c) measurements showed significantly more variation, in part due to lower SNR. This variation is especially evident in the baseline and relaxed periods, wherein the greater plate separation exponentially attenuates the signal. Despite the somewhat noisy baseline signal, tissue blood flow is clearly reduced during each compression period. In Fig 3c, blood flow is reduced by $\sim 90\%$ of baseline level. Blood oxygenation (StO_2 , Fig 3d) exhibited small changes ($\sim 7\%$), but it was consistently smaller under applied load. Tissue scattering (μ'_s , Fig 3e) was observed to change somewhat during the load/relax cycles, increasing during plate separation reduction, and then slowly decreasing during the full compressed period. Water and lipid concentrations (*not plotted*) showed little variation in this subject.

We also attempted to characterize the stress–strain response of the breast with respect to the transition between “compressed” and “baseline” states. We defined an effective strain as the change in plate separation for the two states divided by the initial plate separation ($\Delta d/d_0$, %); we defined an effective stress as the change in measured surface skin pressure (i.e., stress, $\Delta P = P - P_0$, kPa) between compressed and baseline states. The baseline pressure (P_0) was usually quite small, that is, not too different from zero. Across the full range of measurements, the tissue strain and corresponding stress varied over a wide range. Fig 4 shows an example stress change as a function of strain. These example data were collected from a single set of compression events in a single subject. Measurements were thus recorded during the *transition* between the initial period of light contact and the first compression period. At low strains, the relationship between these quantities is approximately linear; at higher strains, the mechanical behavior appears to transition to an exponential dependence similar to that described by Fung (78,79) for uniaxial extension of biomaterials.

Population-averaged Mechanical Properties

We extracted average surface pressure (P) and applied force (F) during each baseline or compressed period for each subject. To account for intersubject variation (e.g., in pressure due to the weight of the breast), we examined only *changes* from baseline in pressure ($\Delta P = P - P_0$) and applied force ($\Delta F = F - F_0$). These baseline pressure (~ 5 kPa) and force (~ 7 N) offsets, however, were quite small compared to the changes in these quantities due to compression.

Comparing all measurements across all subjects, we observe a linear relationship between ΔP and ΔF (Fig 5a), as might be expected. Furthermore, we observed little difference between premenopausal and postmenopausal subjects (*blue and red points*, respectively). This linear relationship suggests that total applied force, which is typically the quantity measured in mammography, may be a good proxy measurement for skin pressure.

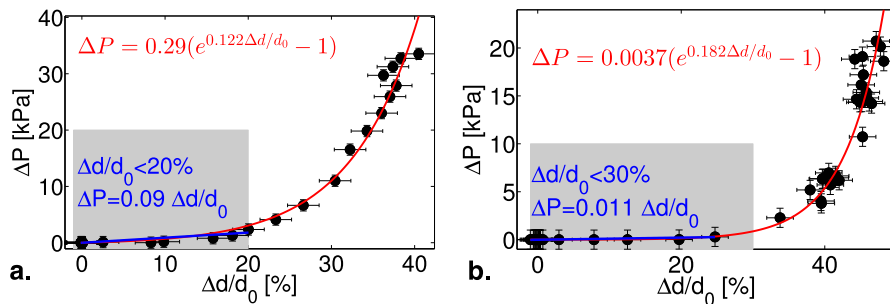


Figure 4. Two examples of stress–strain response during a single compression from baseline load in a pair of subjects. To remove the baseline pressure (e.g., due to the weight of the breast tissue resting on the compression plate), stress is defined as the measured change in surface pressure from the baseline ($\Delta P = P - P_0$, kPa). An effective strain is defined as the measured change in plate separation divided by the initial plate separation ($\Delta d/d_0$, %). Both the quantities were measured continuously; error bars represent the standard deviation of measurements inside a ~ 4 -second averaging time-window. As expected, the stress response in the low strain regimen was approximately linear, and it transitioned to an exponential response at high strain. Note that the linear range differed significantly between subjects. (Color version of the figure is available online.)

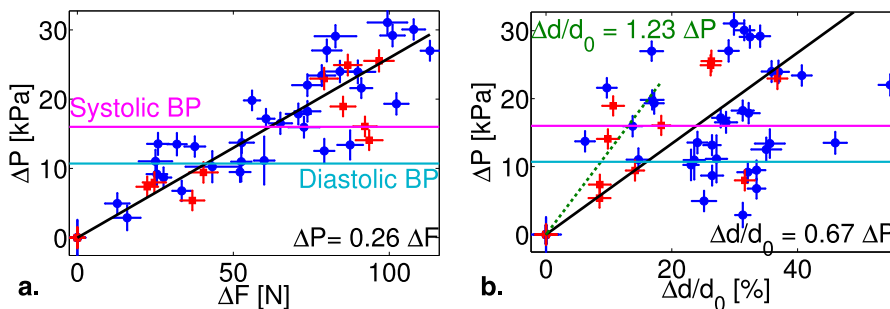


Figure 5. Mechanical properties of breast tissue. Each point corresponds to the average parameter during a baseline or compressed period (e.g., as in Fig 2a); error bars are the standard deviation of the parameter. *Red dots* denote postmenopausal, and *blue dots*, premenopausal subjects. **(a)** Change in surface pressure ($\Delta P = P - P_0$) versus applied force ($\Delta F = F - F_0$) from baseline. **(b)** ΔP (\approx stress) versus fractional change in plate separation ($\Delta d/d_0 \approx$ strain). Note that, we performed linear fits over two ranges of stress: 0%–20% (*green*) and 0%–50% (*black*, all data). Although the latter range includes some data points, which may be outside of the linear stress–strain regimen, we use a simple linear model for the present analysis. Approximate systolic and diastolic blood pressures for healthy persons are shown for reference. For interpretation of the references to color in this figure legend, the reader is referred to the web version of this article.

In Figure 5b, we plot the change in pressure (ΔP) from baseline (i.e., effective stress) as a function of an effective strain, that is, change in compression plate separation divided by the baseline plate separation [$\Delta d/d_0 = (d - d_0)/d_0$]. Since these quantities approximate breast tissue stress and strain during compression, the slope of this curve in the linear regimen can be considered an “effective Young’s modulus” of the breast tissue. Under this approximation, the effective Young’s modulus of the breast tissue measured in this study was 67 kPa (for all data points, 95% confidence interval [CI] 54–80 kPa) or 123 kPa (for data with strains <20%, 95% CI 104–141 kPa); interestingly, these numbers are bracketed by *ex vivo* measurements of Young’s moduli in adipose (~ 17 kPa) and glandular (~ 272 kPa) tissue at 15% strain (10). Note also, in the subjects presented here, we did not discern a significant correlation between the effective Young’s modulus and body mass index.

Population-averaged Physiological Properties

We collected physiological parameters during serial breast compression from 15 subjects (Table 1). The averages of these normalized parameters were computed for each subject in the baseline and compressed time-windows (e.g., Fig 3a), as shown in Figure 6. Averaged over the population, rHb, ΔStO_2 , and $r\mu'_s$ (785 nm) are reduced under external load ($\sim 30\%$, $\sim 20\%$, and $\sim 30\%$; Fig 6a,b,g), but considerable variation in the normalized StO_2 data and μ'_s data are observed at low pressures. Blood flow is significantly reduced during compression ($\sim 90\%$, Fig 6e,f). A slight reduction in lipid concentration is found ($\sim 6\%$, Fig 6c), and the water concentration ($\sim 10\%$, Fig 6d) exhibits a somewhat greater, but less consistent, trend versus applied pressure. Interestingly, rHb, and rBF versus ΔP and ΔF exhibit a saturation effect, that is, reduced response at higher compression.

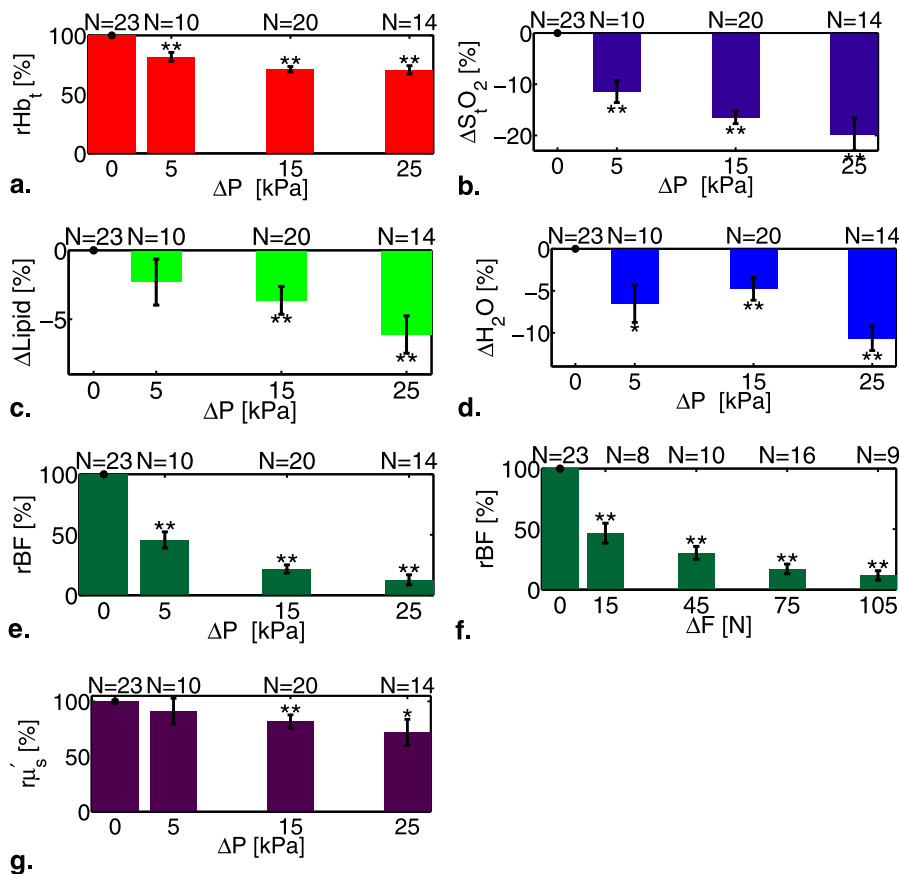


Figure 6. Population-averaged hemodynamic changes under compression versus applied pressure. Percentage change from baseline in (a) total hemoglobin concentration, $rHb_t = Hb_t / (Hb_t)_0$; (b) blood oxygen saturation, $\Delta SO_{t2} = SO_{t2} - (SO_{t2})_0$; (c) lipid concentration, $\Delta \text{lipid} = \text{lipid} - \text{lipid}_0$; (d) water concentration $\Delta H_2O = H_2O - (H_2O)_0$; (e, f) blood flow, $rBF = BF / BF_0$; and (g) tissue reduced scattering coefficient at 785 nm, $r\mu'_s = \mu'_s / (\mu'_s)_0$; under compression versus change in surface pressure $\Delta P = P - P_0$ (a–e, g) or applied force $\Delta F = F - F_0$ (f). Data were binned by $\Delta P =$ baseline (0 kPa), 5 kPa (0–10), 15 kPa (10–20), and 25 kPa (20–30) or $\Delta F =$ baseline (0 N), 15 N (0–30), 45 N (30–60), 75 N (60–90), and 105 N (90–120). Note: data from both compression time windows on both breasts for each subject are included in these figures. Error bars are standard error for each bin; the number of data points included in each bin is noted in the figures. Data marked with “*” (“****”) are statistically different than baseline (zero change) using a two-tailed t test with $P < .05$ (.01). (Color version of the figure is available online.)

DISCUSSION

The data presented here offer insights about the hemodynamics of human breast tissue under external compression at loads similar to those experienced during mammographic imaging. Notably, these studies represent the first DCS-flow measurements detected in *transmission* through human breast. This accomplishment is significant, because the DCS signals are attenuated substantially when traversing large tissue volumes. This, in turn, makes high SNR data acquisition a significant challenge, and such measurements have heretofore not been reported. Furthermore, because full tomographic diffuse optical reconstruction of breast generally requires *transmission* measurements, the results of this study suggest that DCT for optical blood flow imaging in the human breast is accessible with current technology.

Arguably, the most important practical finding of this investigation pertains to imaging techniques that use exogenous contrast agents. A significant reduction in blood flow ($\sim 88\%$) was observed with applied loads of ~ 105 N (~ 25 kPa), that is, loads similar to those arising in x-ray mammography. Moreover, even with “soft” compression [~ 5 kPa surface pressure (~ 20 N)], as used in transmission DOT imaging (21), a reduction in tissue blood flow by $\sim 50\%$ was observed. These changes are presumably due to increased vascular resistance produced by occlusion or partial occlusion of veins, venules, capillaries, arterioles, and even

arteries; such changes should significantly alter injected contrast delivery in clinical DCE-MRI, x-ray tomosynthesis, and digital contrast-enhanced mammography, as well as contrast-enhanced DOT. We note that although both x-ray tomosynthesis (80) and DCE-MRI may be performed at much lower compression than film-based x-ray mammography, similar compressions have been applied by several groups to deliberately modulate breast tissue hemodynamics during imaging (27,40,43,46–48).

Notice that blood flow is not zero ($\sim 10\%$ residual) even at skin pressures above healthy systolic blood pressure (Fig 6e). Most of the subjects included in this study were fairly young and not expected to be hypertensive. However, the breast is not homogeneous; it has complex internal structural elements, which may result in heterogeneous internal pressure. Furthermore, the origin of blood supply to the human breast is highly variable between subjects (81), and this variability in supply (e.g., superficial vs. deep arteries) may also contribute to this effect. Finally, in previous studies of cuff ischemia on the arm, a $\sim 10\%$ residual blood flow was observed in the ischemic state (72). This residue is possibly due to scatter motions in tissue that are not blood flow, such as random motions of red blood cells and other tissue organelles. A portion of these motions has been dubbed biological zero, because it is observed in freshly sacrificed model organisms, such as with laser Doppler flowmetry (82,83). The present study does not measure the true biological zero,

because living tissues will have dynamic signals unrelated to blood flow, although the present study does place an upper bound of $\sim 10\%$ on this parameter.

In a different vein, because DOT imaging derives much of its endogenous contrast from the hemodynamic signals, the observed reductions in Hb_t and StO₂ of $\sim 18\%$ and $\sim 11\%$, respectively, during soft compression can lead to reduced optical imaging contrast. We speculate that these variations are due to expulsion or partial expulsion and trapping of blood in the venous side of the vasculature at high pressure. We observed a reduction in μ'_s of $\sim 30\%$ under high (25 kPa) pressure and significant variation at lower applied pressures. Variations in scattering during diffuse optical measurements are especially significant for continuous-wave measurements, which do not generally measure tissue scattering properties. In total, these observations suggest that pressure monitoring during breast imaging, with both exogenous and endogenous contrast, should be useful for reducing signal variation and for modulating signal contrast.

Because the study probed only healthy breast, we were unable to assess changes in tumor contrast because of compression. We note, however, that tumor growth is often accompanied by angiogenesis—that is, the formation of additional microvasculature in and around the lesion. These tumor blood vessels tend to be less well formed than those in healthy tissue, with leaky and chaotic networks (84). These differences, in fact, offer clinicians unique contrasts that have been the subject of numerous investigations using diffuse optics (24,30,40,42,43,45,47,48,85,86) and other techniques. Given these differences in tissue composition, it is quite likely that tumor vasculature will respond differently to compression perturbations compared to healthy tissue. In future studies, it would be interesting to use DCS in transmission to probe the tumor-bearing breast and thereby study the differential vasculature-related responses to compressional stresses. Such differential responses might be useful for tumor detection and characterization [see, for example, previous studies (43,47,87)].

The investigation also had limited sensitivity to other tissue chromophores, namely water and lipid. Unfortunately, both water and lipid have low absorption at the wavelengths used in this study, and the water and lipid concentration assignments are therefore much less certain than those of HbO₂ and Hb. Nevertheless, the results suggest a slight reduction in tissue lipid concentration and tissue water concentration during compression. We speculate that these lipid reductions could be due to displacement of superficial adipose tissues, which in turn increases the percentage of sampled volume composed of glandular tissue (which has a higher water content). Finally, we note that tissue components without significant absorption at the measured wavelengths (e.g., collagen) were also excluded from this analysis.

Last, with respect to the mechanical properties of breast tissue, we derived some empirical data with the aid of a few simplifying assumptions. Chief among them was to approximate the effective stress–strain relationship as a linear

response, from which an effective Young's modulus was extracted for all data points and all subjects ($Y \sim 67$ kPa, 95% CI 54–80). We observed a range of linear regimes across subjects during compression (e.g., as shown in Fig 4), and a portion of these data points are outside of the linear regimen. A similar analysis for data points from all subjects with strain of $< 20\%$ resulted in a higher effective Young's modulus ($Y \sim 123$, 95% CI 104–141). The average numbers are in rough agreement with the previously published *ex vivo* work on biopsy samples, despite the many complicating factors (geometry, boundary conditions, tissue heterogeneity) in our measurement. We note that Azar et al. (11) suggested that fibroglandular and fatty tissues in the breast become compartmentalized and therefore differ in mechanical properties from isolated excised samples; additionally, work by Lorenzen et al. (88) with magnetic resonance elastography suggests large ($\sim \pm 30\%$) changes in fibroglandular elasticity occur during the course of a woman's menstrual cycle. Despite limitations, we are encouraged by the initial mechanical response data.

CONCLUSIONS

We found that microvascular blood flow in breast tissue was significantly reduced ($\sim 50\%$) with even mild applied force and pressure, such as pressures typically used in “soft compression” breast imaging. At higher compressions, as in use for x-ray mammography, blood flow was reduced by 90% from baseline values. DOT/DOS studies of breast cancer often rely on Hb and HbO₂ contrasts (33); based on our results, the compression applied during imaging may cause significant variation in these chromophore concentrations, both by expelling blood from the breast tissue and by reducing blood flow (and thus oxygen delivery). Thus, in the context of DOT imaging, heterogeneous compression may lead to distorted images and reduced cancer contrast.

More importantly, the results have profound implications for imaging techniques that rely on injected contrast agents. The large change in blood flow during compression that we have observed can significantly reduce contrast agent delivery to breast tissue, or it can force blood-pooling agents out of the breast.

Finally, these results add to the work of others to suggest the possibility of using compression to *enhance* cancer contrast. For example, after injection of targeted contrast agent and a suitable delay time to permit agent binding, compression of the breast could be used to force unbound agent out of the breast tissue, enhancing specificity.

ACKNOWLEDGMENTS

The authors thank Daniel Tien-Nang Chen, Predrag Bakic, Britton Chance, Han Y. Ban, and Saurav Pathak for many helpful discussions during the course of this study. We also thank our research coordinators, Tiffany Averna and Madeline E. Winters, and Nicholas Busch for assistance with the figures. Research support was provided by

National Institutes of Health grants R01-EB002109 (A.G.Y.), P41-RR002305 (A.G.Y., D.R.B.), NTR011U54CA105480 (A.G.Y.), NHLBI HL007915 (D.R.B.), and K99/R00-CA126187 (R.C.). T.D. gratefully acknowledges partial support by Fundació Cellex Barcelona, and D.R.B. acknowledges partial support by the Thrasher Research Fund.

REFERENCES

- Saslow D, Boetes C, Burke W, et al., A. C. S. B. C. A. Group. American Cancer Society guidelines for breast screening with MRI as an adjunct to mammography. *CA-Cancer J Clin* 2007; 57:75–89.
- Niklason LT, Christian BT, Niklason LE, et al. Digital tomosynthesis in breast imaging. *Radiology* 1997; 205:399–406.
- Chen SC, Carton A-K, Albert M, et al. Initial clinical experience with contrast-enhanced digital breast tomosynthesis. *Acad Radiol* 2007; 14: 229–238.
- O'Hagan JJ, Samani A. Measurement of the hyperelastic properties of 44 pathological ex vivo breast tissue samples. *Phys Med Biol* 2009; 54: 2557.
- O'Hagan JJ, Samani A. Measurement of the hyperelastic properties of tissue slices with tumour inclusion. *Phys Med Biol* 2008; 53:7087.
- Samani A, Zubovits J, Plewes D. Elastic moduli of normal and pathological human breast tissues: an inversion-technique-based investigation of 169 samples. *Phys Med Biol* 2007; 52:1565.
- Samani A, Plewes D. A method to measure the hyperelastic parameters of ex vivo breast tissue samples. *Phys Med Biol* 2004; 49:4395.
- Plewes DB, Bishop J, Samani A, et al. Visualization and quantification of breast cancer biomechanical properties with magnetic resonance elastography. *Phys Med Biol* 2000; 45:1591.
- Krouskop TA, Wheeler TM, Kallel F, et al. Elastic moduli of breast and prostate tissues under compression. *Ultrasonic Imaging* 1998; 20:260.
- Wellman P, Howe RD, Dalton E, Kern KA. Breast tissue stiffness in compression is correlated to histological diagnosis. Cambridge, MA: Harvard BioRobotics Laboratory Technical Report, 1999.
- Azar FS, Metaxas DN, Schnall MD. Methods for modeling and predicting mechanical deformations of the breast under external perturbations. *Med Image Anal* 2002; 6:1–27.
- McKnight AL, Kugel JL, Rossman PJ, et al. MR elastography of breast cancer: preliminary results. *AJR Am J Roentgenol* 2002; 178:1411.
- Jacques SL, Pogue BW. Tutorial on diffuse light transport. *J Biomed Opt* 2008; 13:041302. 1–19.
- Durduran T, Choe R, Baker WB, et al. Diffuse optics for tissue monitoring and tomography. *Rep Prog Phys* 2010; 73:076701.
- Enfield LC, Gibson AP, Everdell NL, et al. Three-dimensional time-resolved optical mammography of the uncompressed breast. *Appl Opt* 2007; 46: 3628–3638.
- Poplack SP, Tosteson TD, Wells WA, et al. Electromagnetic breast imaging: results of a pilot study in women with abnormal mammograms. *Radiology* 2007; 243:350–359.
- Nioka S, Yung Y, Shnall M, et al. Optical imaging of breast tumor by means of continuous waves. *Adv Exp Med Biol* 1997; 411:227–232.
- Grosenick D, Wabnitz H, Rinneberg HH, et al. Development of a time-domain optical mammograph and first in vivo applications. *Appl Opt* 1999; 38:2927–2943.
- Spinelli L, Torricelli A, Pifferi A, et al. Characterization of female breast lesions from multi-wavelength time-resolved optical mammography. *Phys Med Biol* 2005; 50:2489–2502.
- Culver JP, Choe R, Holboke MJ, et al. Three-dimensional diffuse optical tomography in the parallel plane transmission geometry: evaluation of a hybrid frequency domain/continuous wave clinical system for breast imaging. *Med Phys* 2003; 30:235–247.
- Choe R, Konecky SD, Corlu A, et al. Differentiation of benign and malignant breast tumors by in-vivo three-dimensional parallel-plate diffuse optical tomography. *J Biomed Opt* 2009; 14:024020.
- Hoogenraad JH, van der Mark MB, Colak SB, Hooft GW, van der Linden ES. First results from the Philips optical mammoscope. In: *Photon Propagation in Tissues III*, Vol 3194. SPIE; 184–190. <http://dx.doi.org/10.1117/12.301053>. Available at: <http://dx.doi.org/10.1117/12.301053>; 1998.
- Nielsen T, Brendel B, Ziegler R, et al. Linear image reconstruction for a diffuse optical mammography system in a noncompressed geometry using scattering fluid. *Appl Opt* 2009; 48:D1–D13.
- Schmitz CH, Klemer DP, Hardin R, et al. Design and implementation of dynamic near-infrared optical tomographic imaging instrumentation for simultaneous dual-breast measurements. *Appl Opt* 2005; 44:2140–2153.
- Intes X, Djeziri S, Ichalalene Z, et al. Time-domain optical mammography softscan: initial results. *Acad Radiol* 2005; 12:934–947.
- Athanasiou A, Vanel D, Fournier L, et al. Optical mammography: a new technique for visualizing breast lesions in women presenting non palpable BIRADS 4–5 imaging findings: preliminary results with radiologic–pathologic correlation. *Canc Imag* 2007; 7:34.
- Fournier LS, Vanel D, Athanasiou A, et al. Dynamic optical breast imaging: a novel technique to detect and characterize tumor vessels. *Eur J Rad* 2009; 69:43–49.
- Durduran T, Choe R, Culver JP, et al. Bulk optical properties of healthy female breast tissue. *PMB* 2002; 47:2847–2861.
- Spinelli L, Torricelli A, Pifferi A, et al. Bulk optical properties and tissue components in the female breast from multiwavelength time-resolved optical mammography. *J Biomed Opt* 2004; 9:1137–1142.
- Fang Q, Carp SA, Selb J, et al. Combined optical imaging and mammography of the healthy breast: optical contrast derived from breast structure and compression. *IEEE Trans Med Imaging* 2009; 28:30–42.
- Taroni P, Bassi A, Comelli D, et al. Diffuse optical spectroscopy of breast tissue extended to 1100 nm. *J Biomed Opt* 2009; 14:054030.
- Taroni P, Pifferi A, Salvagnini E, et al. Seven-wavelength time-resolved optical mammography extending beyond 1000 nm for breast collagen quantification. *Opt Exp* 2009; 17:15932–15946.
- Leff DR, Warren OJ, Enfield LC, et al. Diffuse optical imaging of the healthy and diseased breast: a systematic review. *Breast Cancer Res Treat* 2008; 108:9–22.
- Srinivasan S, Pogue BW, Carpenter C, et al. Developments in quantitative oxygen-saturation imaging of breast tissue in vivo using multispectral near-infrared tomography. *Antioxid Redox Signal* 2007; 9:1143–1156.
- Shah N, Cerussi AE, Jakubowski D, et al. Spatial variations in optical and physiological properties of healthy breast tissue. *J Biomed Opt* 2004; 9: 534–540.
- Blyschak K, Simick M, Jong R, et al. Classification of breast tissue density by optical transillumination spectroscopy: optical and physiological effects governing predictive value. *Med Phys* 2004; 31:1398–1414.
- Blackmore KM, Knight JA, Jong R, et al. Assessing breast tissue density by transillumination breast spectroscopy (TIBS): an intermediate indicator of cancer risk. *Br J Radiol* 2007; 80:545–556.
- Blackmore KM, Knight JA, Lilge L. Association between transillumination breast spectroscopy and quantitative mammographic features of the breast. *Cancer Epidemiol Biomarkers* 2008; 17:1043.
- Taroni P, Pifferi A, Quarto G, et al. Noninvasive assessment of breast cancer risk using time-resolved diffuse optical spectroscopy. *J Biomed Opt* 2010; 15:060501.
- Jiang S, Pogue BW, Paulsen KD, et al. In vivo near-infrared spectral detection of pressure-induced changes in breast tissue. *Opt Lett* 2003; 28: 1212–1214.
- Nioka S, Wen S, Zhang J, et al. Simulation study of breast tissue hemodynamics during pressure perturbation. *Adv Exp Med Biol* 2005; 566:17–22.
- Carp SA, Kauffman T, Fang Q, et al. Compression-induced changes in the physiological state of the breast as observed through frequency domain photon migration measurements. *J Biomed Opt* 2006; 11:064016.
- Xu RX, Qiang B, Mao JJ, et al. Development of a handheld near-infrared imager for dynamic characterization of in vivo biological tissue systems. *Appl Opt* 2007; 46:7442–7451.
- Boverman G, Fang Q, Carp SA, et al. Spatio-temporal imaging of the hemoglobin in the compressed breast with diffuse optical tomography. *Phys Med Biol* 2007; 52:3619–3641.
- Carp SA, Selb J, Fang Q, et al. Dynamic functional and mechanical response of breast tissue to compression. *Opt Exp* 2008; 16: 16064–16078.
- Jiang SD, Pogue BW, Laughney AM. Measurement of pressure-displacement kinetics of hemoglobin in normal breast tissue with near-infrared spectral imaging. *Appl Opt* 2009; 48.
- Al abdi R, Graber HL, Xu Y, et al. Optomechanical imaging system for breast cancer detection. *JOSA A* 2011; 28:2473–2493.

48. Flexman M, Khalil M, Al Abdi R, et al. Digital optical tomography system for dynamic breast imaging. *J Biomed Opt* 2011; 16:076014.
49. Boas DA, Campbell LE, Yodh AG. Scattering and imaging with diffusing temporal field correlations. *Phys Rev Lett* 1995; 75:1855–1858.
50. Choe R, Durduran T. Diffuse optical monitoring of the neoadjuvant breast cancer therapy. *IEEE J Sel Topics Quantum Electron* 2012; 18:1367–1386.
51. Boas DA, Yodh AG. Spatially varying dynamical properties of turbid media probed with diffusing temporal light correlation. *JOSA A* 1997; 14:192–215.
52. Durduran T, Choe R, Yu GQ, et al. Diffuse optical measurement of blood flow in breast tumors. *Opt Lett* 2005; 30:2915–2917.
53. Zhou C, Choe R, Shah N, et al. Diffuse optical monitoring of blood flow and oxygenation in human breast cancer during early stages of neoadjuvant chemotherapy. *J Biomed Opt* 2007; 12:051903.
54. Menon C, Polin GM, Prabhakaran I, et al. An integrated approach to measuring tumor oxygen status using human melanoma xenografts as a model. *Cancer Res* 2003; 63:7232–7240.
55. Roche-Labarbe N, Carp SA, Surova A, et al. Noninvasive optical measures of CBV, STO2, CBF index, and RCMRO2 in human premature neonates' brains in the first six weeks of life. *Hum Brain Mapp* 2010; 31:341–352.
56. Sunar U, Makonnen S, Zhou C, et al. Hemodynamic responses to antivasculature therapy and ionizing radiation assessed by diffuse optical spectroscopies. *Optics Express* 2007; 15:15507–15516.
57. Li J, Ninck M, Koban L, et al. Transient functional blood flow change in the human brain measured noninvasively by diffusing-wave spectroscopy. *Opt Lett* 2008; 33:2233–2235.
58. Dietsche G, Ninck M, Ortoft C, et al. Fiber-based multispeckle detection for time-resolved diffusing-wave spectroscopy: characterization and application to blood flow detection in deep tissue. *Appl Opt* 2007; 46:8506–8514.
59. Jaillon F, Li J, Dietsche G, et al. Activity of the human visual cortex measured non-invasively by diffusing-wave spectroscopy. *Optics Express* 2007; 15:6643–6650.
60. Jaillon F, Skipetrov SE, Li J, et al. Diffusing-wave spectroscopy from head-like tissue phantoms: influence of a non-scattering layer. *Optics Express* 2006; 14:10181–10194.
61. Durduran T. Noninvasive measurements of tissue hemodynamics with hybrid diffuse optical methods. PhD thesis. Philadelphia, PA, USA: University of Pennsylvania, 2004.
62. Durduran T, Yu G, Burnett MG, et al. Diffuse optical measurement of blood flow, blood oxygenation, and metabolism in a human brain during sensorimotor cortex activation. *Opt Lett* 2004; 29:1766–1768.
63. Cheung C, Culver JP, Takahashi K, et al. In vivo cerebrovascular measurement combining diffuse near-infrared absorption and correlation spectroscopies. *Phys Med Biol* 2001; 46:2053.
64. Yu GQ, Durduran T, Zhou C, et al. Noninvasive monitoring of murine tumor blood flow during and after photodynamic therapy provides early assessment of therapeutic efficacy. *Clin Cancer Res* 2005; 11:3543–3552.
65. Buckley EM, Cook NM, Durduran T, et al. Cerebral hemodynamics in preterm infants during positional intervention measured with diffuse correlation spectroscopy and transcranial Doppler ultrasound. *Optics Express* 2009; 17:12571–12581.
66. Durduran T, Zhou C, Buckley EM, et al. Optical measurement of cerebral hemodynamics and oxygen metabolism in neonates with congenital heart defects. *J Biomed Opt* 2010; 15:037004.
67. Yu G, Floyd TF, Durduran T, et al. Validation of diffuse correlation spectroscopy for muscle blood flow with concurrent arterial spin labeled perfusion MRI. *Optics Express* 2007; 15:1064–1075.
68. Kim M, Durduran T, Frangos S, et al. Noninvasive measurement of cerebral blood flow and blood oxygenation using near-infrared and diffuse correlation spectroscopies in critically brain-injured adults. *Neurocrit Care* 2010; 12:173–180.
69. Zhou C, Eucker SA, Durduran T, et al. Diffuse optical monitoring of hemodynamic changes in piglet brain with closed head injury. *J Biomed Opt* 2009; 14:034015.
70. Zhou C, Yu G, Daisuke F, et al. Diffuse optical correlation tomography of cerebral blood flow during cortical spreading depression in rat brain. *Optics Express* 2006; 14:1125–1144.
71. Durduran T, Zhou C, Edlow BL, et al. Transcranial optical monitoring of cerebrovascular hemodynamics in acute stroke patients. *Optics Express* 2009; 17:3884–3902.
72. Yu GQ, Durduran T, Lech G, et al. Time-dependent blood flow and oxygenation in human skeletal muscles measured with noninvasive near-infrared diffuse optical spectroscopies. *J Biomed Opt* 2005; 10:024027. 1–12.
73. Yu G, Durduran T, Zhou C, et al. Real-time in situ monitoring of human prostate photodynamic therapy with diffuse light. *Photochem Photobiol* 2006; 82:1279–1284.
74. Sunar U, Quon H, Durduran T, et al. Noninvasive diffuse optical measurement of blood flow and blood oxygenation for monitoring radiation therapy in patients with head and neck tumors: a pilot study. *J Biomed Opt* 2006; 11:064021.
75. Busch DR. Computer-aided, multi-modal, and compression diffuse optical studies of breast tissue. PhD thesis. Philadelphia, PA: University of Pennsylvania, 2011.
76. O'Leary D, Grant T, Rainford L. Image quality and compression force: the forgotten link in optimisation of digital mammography? *BCR* 2011; 13:P10.
77. Mourant JR, Fuselier T, Boyer J, et al. Predictions and measurements of scattering and absorption over broad wavelength ranges in tissue phantoms. *App Opt* 1997; 36:949–957.
78. Fung YC. *Biomechanics: mechanical properties of living tissue*. New York, NY: Springer-Verlag, 1981.
79. Humphrey J. Review paper: continuum biomechanics of soft biological tissues. *Proc R Soc Lond Ser A Math Phys Eng Sci* 2003; 459:3.
80. Förnvik D, Dustler M, Andersson I, et al. Pressure distribution in mammography: compression of breasts with malignant tumor masses. *SPIE Med Imaging Int Soc Optics Photonics*, 2013; 86684E.
81. Doughty JC, McCarter DHA, Kane E, et al. Anatomical basis of intra-arterial chemotherapy for patients with locally advanced breast cancer. *Br J Surg* 1996; 83:1128–1130.
82. Liebert A, Maniewski R. Influence of probe optical arrangement on biological zero in laser-doppler perfusion measurements. In: *Engineering in Medicine and Biology Society, 1996. Bridging Disciplines for Biomedicine. Proceedings of the 18th Annual International Conference of the IEEE, Vol 1*. IEEE, 1997; 200–201.
83. Zhong J, Seifalian AM, Salerud GE, et al. A mathematical analysis on the biological zero problem in laser Doppler flowmetry. *IEEE Trans Biomed Eng* 1998; 45:354–364.
84. Jain RK. Molecular regulation of vessel maturation. *Nat Med* 2003; 9:685–693.
85. Dixit SS, Kim H, Comstock C, et al. Near infrared transillumination imaging of breast cancer with vasoactive inhalation contrast. *Biomed Opt Exp* 2010; 1:295–309.
86. Flexman ML, Kim HK, Gunther JE, et al. Optical biomarkers for breast cancer derived from dynamic diffuse optical tomography. *J Biomed Opt* 2013; 18:096012.
87. Zhang GJ. *DOBI Comfortscan System Clinical Effectiveness Evaluation Report, Technical Report*. DOBI Medical International. Available at: http://dobiglobal.com/pdfs/DOBIComfortScan_Clinical_Report_2011.pdf; 2011.
88. Lorenzen J, Sinkus R, Biesterfeldt M, et al. Menstrual-cycle dependence of breast parenchyma elasticity: estimation with magnetic resonance elastography of breast tissue during the menstrual cycle. *Investig Radiol* 2003; 38:236.
89. Contini D, Martelli F, Zaccanti G. Photon migration through a turbid slab described by a model based on diffusion approximation. I. theory. *Appl Opt* 1997; 36:4587–4599.
90. Carp SA, Dai GP, Boas DA, et al. Validation of diffuse correlation spectroscopy measurements of rodent cerebral blood flow with simultaneous arterial spin labeling MRI; towards MRI-optical continuous cerebral metabolic monitoring. *Biomed Opt Express* 2010; 1:553–565.

APPENDIX A. OPTICAL DATA ANALYSIS

The least squares fitting procedure we used to extract information about tissue chromophore concentration and tissue scattering from the TD-DOS data was straightforward. On the theoretical side, we computed transmission temporal point spread functions from the homogeneous slab solution to the diffusion equation (89) at each wavelength; the inputs to these functions were the tissue $\mu'_s(\lambda)$ and $\mu_a(\lambda)$, which in turn depend on tissue HbO₂, Hb, lipid, H₂O, A , and b as described in the main text. These calculated point spread functions were then convoluted with the measured

instrument response functions at each wavelength to generate $T^c(t, \lambda)$, the expected transmission pulses as a function of wavelength and time.

We then iteratively minimized the difference between the measured transmission ($T(t, \lambda)$) and these calculated temporal response curves, using a standard iterative least squares minimization algorithm with the error function

$$\chi^2 = \sum_{\lambda, t} \left(\frac{T(t, \lambda) - T^c(t, \lambda)}{\sqrt{T(t, \lambda)}} \right)_{n_i}^{t_2} \quad (\text{A.1})$$

The fit limit time t_1 (t_2) corresponds to the point at which the rising (falling) point spread function is equal to 50% (0.5%) of its peak value. (We note that the single wavelength homogeneous slab solution to the diffusion equation depends in important ways on four parameters: μ'_s , μ_a , peak amplitude, and a time offset.) By fitting data collected at all six wavelengths simultaneously, we derive a single minimization function that depends directly on HbO_2 , Hb , lipid, H_2O , A , and b ; with this approach, we were able to reduce the number of free parameters for the total fitting routine from 24 to 18 (including amplitude and time offset parameters). This reduction in free parameters stabilized our fitting routines.

The procedures we followed to extract tissue blood flow indices were also straightforward. They are described at length in a recent review (14). The theoretical model again (as in the case of TD-DOS) used solutions to the diffusion equation in the homogeneous infinite slab geometry; although the diffusion equation of interest in the present case is the so-called correlation diffusion equation (14), its solutions are formally identical to those of the traditional photon diffusion equation. Thus, by analogy to the frequency domain solution to the diffusion equation in the transmission infinite slab geometry (14), the theoretical prediction for the measured correlation function is very closely related to the infinite slab Green's function for the electric field autocorrelation function. This function depends on several parameters, including the correlation decay time τ that is,

$$G_{\text{slab}}^{\text{dcs}}[\tau] = \frac{1}{4\pi} \sum_{m=-\infty}^{\infty} \left(r_{1,m}^{-1} e^{-k_{\text{dcs}}(\tau)r_{1,m}} - r_{2,m}^{-1} e^{-k_{\text{dcs}}(\tau)r_{2,m}} \right) \quad (\text{A.2})$$

With the parameters

$$r_{1,m} = \sqrt{\rho^2 + z_{1,m}^2} \quad (\text{A.3})$$

$$r_{2,m} = \sqrt{\rho^2 + z_{2,m}^2} \quad (\text{A.4})$$

$$z_{1,m} = d(1 - 2m) - 4mz_b - z_0 \quad (\text{A.5})$$

$$z_{2,m} = d(1 - 2m) - (4m - 2)z_b + z_0 \quad (\text{A.6})$$

$$z_0 = \frac{1}{\mu'_s + \mu_a} \approx \frac{1}{\mu'_s} \quad (\text{A.7})$$

$$z_b = \frac{2z_0}{3} \frac{1 + R_{\text{eff}}}{1 - R_{\text{eff}}} \quad (\text{A.8})$$

$$k_{\text{dcs}}(\tau) = \sqrt{\frac{\nu}{D} \left(\mu_a + \frac{\alpha \mu'_s \kappa_0^2 \langle \Delta r^2(\tau) \rangle}{3} \right)} \quad (\text{A.9})$$

$$\kappa_0 = \frac{2\pi n}{\lambda} \quad (\text{A.10})$$

$$D = \frac{\nu}{3(\mu'_s + \mu_a)} \approx \frac{\nu}{3\mu'_s} \quad (\text{A.11})$$

where d is the slab thickness, ρ the transverse source-detector separation, ν is the speed of light, n is the index of refraction, R_{eff} is the Fresnel reflection coefficient at the slab boundaries, and α is the fraction of moving scatterers. Note, this fit uses the optical properties (μ_a and μ'_s) at the DCS wavelength (785 nm) determined from TD-DOS measurements.

Various researchers have found that the mean square particle displacement [$\langle \Delta r^2(\tau) \rangle$] in biological tissue is best described with a Brownian model (52,53,72,74,63,90)—that is, $\langle \Delta r^2[\tau] \rangle = 6D_B\tau$, where D_B is an *effective* diffusion coefficient that is several orders of magnitude larger than the thermal (Einstein) coefficient for particles of the size of red blood cells; see Durduran et al. (14) for a discussion of D_B . In this case of “effective” Brownian motion,

$$k_{\text{dcs}}^2[\tau] = \frac{\nu}{D} (\mu_a + 2\mu'_s \kappa_0^2 \alpha D_B \tau) \quad (\text{A.12})$$

The temporal autocorrelation data are thus fit to derive the factor, αD_B , which we define as the blood flow index (BF). This BF, αD_B , has been demonstrated to provide a useful quantitative measure of tissue blood flow and changes thereof in a variety of tissues and during a variety of physiological perturbations (61–74).